ARTICLE

Impact of Varying Side Chain Structure on Organic Electrochemical Transistor Performance: A Series of Oligoethylene Glycol-substituted Polythiophenes

Received 00th January 20xx,
Accepted 00th January 20xx

DOI: 10.1039/x0xx00000x

Shinya E. Chen,[a] Lucas Q. Flagg,[b†] Jonathan W. Onorato,[c†] Lee J. Richter,[b] Jiajie Guo,[a] Christine K. Luscombe,[acde] David S. Ginger[ad]**

The electrochemical doping/dedoping kinetics, and the organic electrochemical transistor (OECT) performance of a series polythiophene homopolymers with ethylene glycol units in their side chains using both kosmotropic and chaotropic anion solutions were studied. We compare their performance to a reference polymer, the polythiophene derivative with diethylene glycol side chains, poly(3-{[2-(2-methoxyethoxy)ethoxy]methyl}thiophene-2,5-diyl) (P3MEEMT). We find larger OECT material figure of merit, μC^*, where μ is the carrier mobility and C^* the volumetric capcitance, and faster doping kinetics with more oxygen atoms on the side chains, and if the oxygen atom is farther from the polythiophene backbone. Replacing the oxygen atom close to the polythiophene backbone with an alkyl unit increases the film π-stacking crystallinity (higher electronic conductivity in undoped film) but sacrifices the available doping sites (lower volumetric capacitance C^* in OECT). We show that this variation in C^* is the dominant factor in changing the μC^* product for this family of polymers. With more oxygen atoms on the side chain, or with the oxygen atom farther from the polymer backbone, we observe both more passive swelling and higher C^*. In addition, we show that, compared to the doping speed, the dedoping speed, as measured via spectroelectrochemistry, is both generally faster and less dependent on ion species or side chain oxygen content. Last, through OECT, electrochemical impedance spectroscopy (EIS) and spectroelectrochemistry measurements, we show that the chaotropic anion PF_6^- facilitates higher doping levels, faster doping kinetics, and lower doping thresholds compared to the kosmotropic anion Cl^-, although the exact differences depend on the polymer side chains. Our results highlight the importance of balancing μ and C^* when designing molecular structure for OECT active layer.

1. Introduction

Conjugated polymers with mixed ionic-electronic conduction properties, or organic mixed ionic-electronic conductors (OMIECs), are promising materials being explored in the fields of bioelectronics,[1,2] neuromorphic computing,[3,4] and energy storage.[5] In the field of bioelectronics and neuromorphic computing, organic electrochemical transistors (OECTs) provide a device configuration that can transduce small changes in an ionic flux into large changes in electrical current.[6–8] An OECT is a three-terminal device with source and drain electrodes connected by a channel active layer (conjugated polymer), and with an electrolyte solution in between the channel active layer and the gate electrode. The working principle of an OECT (in accumulation mode) involves the injection of polarons from the source electrode into the channel driven by the gate potential bias (V_G) and a concomitant change in electrolyte balance in the polymer film (both anion injection and cation expulsion for p-type material) to maintain charge neutrality.[9] This coupled process of electrochemical charging (commonly referred to as "electrochemical doping") results in the volume of the polymer film filled with charged polarons, which are in turn charge-compensated by ions from the electrolyte. The density of electronic carriers (polarons) in the active channel, and hence the magnitude of the electrical current that flows through the channel (I_D) is modulated by V_G. The resulting change in drain current I_D that is achieved by a given change in V_G is reported as the transconductance ($g_m \equiv \boldsymbol{\partial I_D / \partial V_G}$). As a class of transistors, OECTs offer several attractive properties including high g_m (≈ mS), low device operation voltages (< |1 V|), and the ability to transduce ionic action potentials (voltages) in biological environments ranging from neurons in the brain[8,10] to carnivorous plants.[11]

To compare the performance of different OMIECs as an OECT active layer in a manner that is unaffected by factors such as transistor device geometry and operation voltage, Inal and colleagues proposed using the product of electronic carrier mobility (μ) and the volumetric capacitance (C^*) as a figure of merit to evaluate different OECT materials.[12,13] The μC^* product captures the

[a] Molecular Engineering and Science Institute, University of Washington, Seattle, WA 98195, United States.
[b] Materials Science and Engineering Division, National Institute of Standards and Technology, Gaithersburg, Maryland 20899, United States.
[c] Department of Materials Science and Engineering, University of Washington, Seattle, WA 98195, United States.
[d] Department of Chemistry, University of Washington, Seattle, WA 98195, United States.
[e] Current Address: pi-Conjugated Polymers Unit, Okinawa Institute of Science and Technology Graduate University, Onna-son, Okinawa, 904-0495, Japan.
† These two authors contributed equally to the work.
* Corresponding Authors. E-mail christine.luscombe@oist.jp, dginger@uw.edu
Electronic Supplementary Information (ESI) available. See DOI: 10.1039/x0xx00000x

steady-state ionic/electronic transport process under device operation. The expected relationship between the μC^* product and g_m in the transistor saturation regime is given in Eq. 1:[12,13]

$$g_m \cong \mu C^* \cdot \frac{Wd}{L} \cdot (V_T - V_G) \quad (1)$$

The value of μC^* can thus be extracted by measuring the g_m of different OECTs and performing a linear regression between g_m and $(Wd/L) \cdot (V_G - V_T)$, as the channel width (W), length (L), channel active layer thickness (d), threshold voltage (V_T) and V_G are known. The μC^* of the classical OECT material Poly(3,4-ethylenedioxythiophene): polystyrenesulfonate (PEDOT:PSS) without any pre or postprocessing is ≈ 50 F cm^{-1} V^{-1} s^{-1}.[13] This is a relatively high value that results from a combination of high electronic mobility and moderate volumetric capacitance. PEDOT:PSS is the most widely used OECT material because of its commercial availability, operational stability and relatively high OECT performance. Typically, an OECT with PEDOT:PSS active layer is operated in depletion mode, meaning the I_D is at on-state when no V_G applied. Depletion mode OECT is less desirable in applications requires low-power consumption.

Over the last few years, researchers have been searching for new polymers with improved OECT performance.[14,15] Desirable targets include materials with high μC^* products,[16–19] those that can operated in accumulation mode,[17,20–22] and those that show faster kinetics.[3,23,24] Among different synthetic approaches, the strategy of modifying the polymer side chains has been applied extensively on different conjugated backbones with the goal of realizing new OMIECs that operate as accumulation mode OECTs with μC^* comparable to or higher than PEDOT:PSS. Notably, conferring conjugated polymers with fully glycolated side chain has become a ubiquitous strategy to enable higher μC^*.[17,25–27]

Previously, we compared the OECT performance of a polythiophene with fully alkylated side chain, poly(3-hexylthiophene-2,5-diyl) (P3HT), and a polythiophene with fully glycolated side chain, poly(3-{[2-(2-methoxyethoxy)ethoxy]methyl}thiophene-2,5-diyl) (P3MEEMT).[28] While P3MEEMT shows a higher μC^* product than P3HT, the mobility of P3MEEMT, like other polymers with ethylene glycol side chains, showed a complex relationship between polymer crystallinity, dry hole mobility, and hole mobility in the hydrated OECT.[22,28,29] Thus, given the known trade-offs between morphology, ion injection, and carrier mobility,[30] it is interesting to consider if there is room to compromise between degree of hydration and crystallinity, to achieve a beneficial compromise between the large volumetric capacitance and favorable kinetics achievable with readily hydrated polymers with high ethylene glycol (EG) content, and favorable ordering and hole mobility of hydrophobic P3HT with only alkyl chains.

Recently, Luscombe and co-workers reported the synthesis of a related family of polythiophenes with varying degrees of ethylene glycol (EG) content in the side chains, as well as varying positions that are suitable for testing this hypothesis.[31] They characterized the performance of these materials as polymer electrolytes for Li-ion batteries, hypothesizing that ionic, electronic, and balanced conduction could be improved by meticulously varying EG unit content and position in the polythiophene side chain. They found further that both ionic and electronic conductivity could be improved by increasing the oxygen atom distance from the polythiophene backbone.[31]

Here, we explore the performance of these materials in OECT applications, with the goal of testing if it is possible to achieve a more optimal compromise between volumetric capacitance, kinetics, and carrier mobility in hydrated OECTs. Specifically, we test the OECT performance of three reduced-oxygen-content side chain polymers in both chaotropic and kosmotropic electrolytes and compare the results to the aforementioned reference polymer, P3MEEMT. This study emphasizes the very different nature of OMIECs operated in dry and hydrated states and bridges the gap between our understanding of conjugated homopolymers with pure alkyl and fully glycolated side chain in terms of their OECT performance.

2. Experimental

2.1 Chemicals

Potassium chloride (KCl), potassium hexafluorophosphate (KPF_6), potassium trifluoromethanesulfonimide (KTFSI) and chlorobenzene were purchased from Sigma-Aldrich. All other chemicals unless otherwise specified were obtained from Sigma-Aldrich and used as received.

2.2 Polymer Synthesis

The detailed monomer and polymer synthesis are described in the previous studies. [28,31]

2.3 Sample Preparation

All polymers were dissolved in chlorobenzene and stirred overnight at 50 °C. The concentration of polymer solution is 20 mg/mL. The substrates were cleaned sequentially by sonication in acetone and isopropanol for 15 min each. The surface of the substrate was then treated with oxygen plasma for 3 min before spin coating at 1000 rpm (1 rpm = 2π/60 rad/s) for 60 s. All electrolytes were made with Milli-Q water. All electrolytes were degassed before measurements. We degassed the electrolytes via sparing nitrogen gas into solution (≈ 10 mL) for over 10 min.

2.4 Spectroelectrochemistry

The ultraviolet-visible, UV-Vis, absorption spectra at different doping potential and the electrochemical doping and dedoping kinetics were measured using a Metrohm Autolab PGSTAT204 (with NOVA Software version 2.1) coupled with an Agilent 8453 spectrometer. Polymer was spun casted onto fluoride-doped tin oxide-coated glass (FTO, Sigma-Aldrich, 7 Ω/sq) and was used as a working electrode. A Ag/AgCl electrode and a Pt mesh was used as reference electrode and counter electrode, respectively. All three electrodes were submerged into a cuvette containing either 100 mmol/L $KCl_{(aq)}$ or $KPF_{6(aq)}$. UV-Vis measurements were collected with an integration time of 0.1 s/spectrum. The decay of the π-π* absorption (Abs) peak over time during electrochemical doping is fit to the biexponential function: $Abs(t) = a_1 \cdot e^{-t/\tau_1} + a_2 \cdot e^{-t/\tau_2}$. And the doping time constant is defined as $a_1 \cdot \tau_1 + a_2 \cdot \tau_2$. The recovery of the π-π* absorption peak over time during dedoping is fit to the biexponential

function: Abs(t) = $b_1 \cdot (1- e^{-t/\tau_1}) + b_2 \cdot (1- e^{-t/\tau_2})$. And the dedoping time constant is defined as $b_1 \cdot \tau_1 + b_2 \cdot \tau_2$.

2.5 Organic Electrochemical Transistor (OECT) Device Fabrication and Characterization

OECT devices comprised lithographically patterned gold on glass substrates (see lithography process below) with transistor lengths of 10 µm and widths ranging from 100 µm to 4000 µm. Reduced-oxygen-content side chain polymers were spun casted onto OECT substrates and were carefully removed except at the electrode junction region via cotton tips under microscope. Cotton tips were slightly dampened with acetone solution. An insulating layer containing cellulose acetate and acrylates copolymer (Nail polish: Sally Hansen, Insta-Dri Top Coat) was then applied to avoid the direct contact between electrode and electrolyte during further characterizations. Devices were measured in degassed electrolytes. The electrolyte (≈ 1 mL) was contained in a polydimethylsiloxane (PDMS) reservoir during OECT measurements. The assembly of the OECT substrate, the PDMS reservoir and the electrical connections were achieved via a 3D-printed holder. Transfer curves were measured by varying V_G from 0 V to -0.7 V and then back to 0 V (vs. Ag/AgCl). The V_D was fixed at -0.6 V. For KCl electrolyte, the step size of V_G was either 0.01 V with 5 s between each step or 0.05 V with 20 s between each step. For KPF_6 electrolyte, the step size of V_G was 0.01 V with 2.5 s between each step or 0.05 V with 10 s between each step to ensure reaching steady-state and minimizing hysteresis between forward and backward scans.

The detailed lithography process: NR9-3000PY negative resist (Futurrex, Inc.) was deposited on cleaned glass wafers with diameter equals to 0.1016 m (University Wafer, Inc.) through spin-coating, followed by UV light exposure (ABM-SemiAuto-Aligner) and resist development. Metal deposition (10 nm chromium or titanium and 100 nm gold) was accomplished through sputtering (Evatec LLS EVO Sputter System) or evaporation (CHA Solution e-beam evaporator). The resist lift-off was achieved by soaking wafers in acetone solution overnight. The wafers were then diced using a Disco Wafer Dicer (Disco, America).

2.6 Electrochemical Impedance Spectroscopy (EIS) for C^* Determination

EIS measurements were performed on gold-coated glass substrates with a defined area of (0.01 or 0.04) cm^2. Polymers were spun casted on the gold substrates. A Ag/AgCl electrode and a Pt mesh was used as reference electrode and counter electrode, respectively. The polymer was first electrochemically doped at specific direct current (DC) potential bias (ranging from 0.2 V to 0.7 V vs Ag/AgCl) for 60 s (unless otherwise specified), and the alternating current (AC) perturbation (Sine wave with 10 mV amplitude and frequency from 10^5 Hz to 10^{-1} Hz) was then performed on top of the DC potential bias. The obtained EIS data was fit to either a Randles circuit[32,33] or a Kovac's circuit.[33,34] Fitting was performed with the Metrohm NOVA software or Python impedance.py package.[35] The definition of χ^2 in this study:

$$\chi^2 = \left(\sum_{i=1}^{n} \frac{\left[\left(Z_{Re,Data} - Z_{Re,Fit}\right)^2 + \left(Z_{Img,Data} - Z_{Img,Fit}\right)^2\right]}{\left(Z_{Re,Data}{}^2 + Z_{Img,Data}{}^2\right)}\right)/(n - m) \quad (2)$$

Where n is the number of data points and m is the number of adjustable parameters in the fit (number of circuit element in the equivalent circuit). $Z_{Re,Data}$ and $Z_{Re,Fit}$ represent the measured and fitted real part of impedance. $Z_{Img,Data}$ and $Z_{Img,Fit}$ represent the measured and fitted imaginary part of impedance, respectively.

2.7 Quartz Crystal Microbalance with Dissipation (QCM-D)

QCM-D measurements were conducted using a Q-sense Explorer (Biolin Scientific) on gold/titanium coated sensors. Passive swelling was calculated the following way. First, we recorded the frequency of the bare gold coated sensor in air and subsequently in deionized (DI) water. The crystal was then removed, and polymer solutions were spin coated onto the premeasured sensor. We then measured the polymer coated sensor in both air and DI water. Using the "stitch data" function of the QSoft401 software, we compared the frequency of the bare and coated sensor. The thickness of polymer layer in both air and water were computed using the Sauerbrey equation:[36]

$$\Delta m = \frac{-17.7}{n} \Delta f_n \quad (3)$$

Where Δm is the areal mass, n is the overtone number and Δf_n is the change is frequency at the n^{th} overtone. We assumed the density of polymers are 1100 kg/m^3.

2.8 Cyclic Voltammetry (CV)

Cyclic voltammetry measurements were conducted using Metrohm Autolab PGSTAT204 potentiostat. Polymer was spun casted on the gold substrate and used as a working electrode. A Ag/AgCl electrode and a Pt mesh was used as reference electrode and counter electrode, respectively. The scan rate used is 50 mV/s.

2.9 Atomic Force Microscopy (AFM)

AFM data, including topography and scratch edge images for film thickness measurements, were acquired on an MFP-3D. Polymers were deposited on either FTO or glass substrate.

2.10 Contact Angle Measurement

Contact angle measurements were conducted using the custom-built setup with a CCD camera a height adjustable stage. The images were analyzed using the FTA32 software.

2.11 P3MEEMT Data

P3MEEMT data, except for QCM swelling measurements, contact angle measurements and AFM measurements, were obtained from our previous study and used directly for comparison to the reduced-oxygen-content side chain polymers.[28]

3. Results and Discussion

3.1. OECT Device Performance

We first studied the performance of the reduced-oxygen-content side chain polymers in OECTs. Figure 1a shows the OECT device structure used for testing. Figure 1b shows the chemical structures of the reduced-oxygen-content side chain polymers studied. Poly(3-(methoxyethoxybutyl)thiophene), or P3APPT, has two oxygen atoms

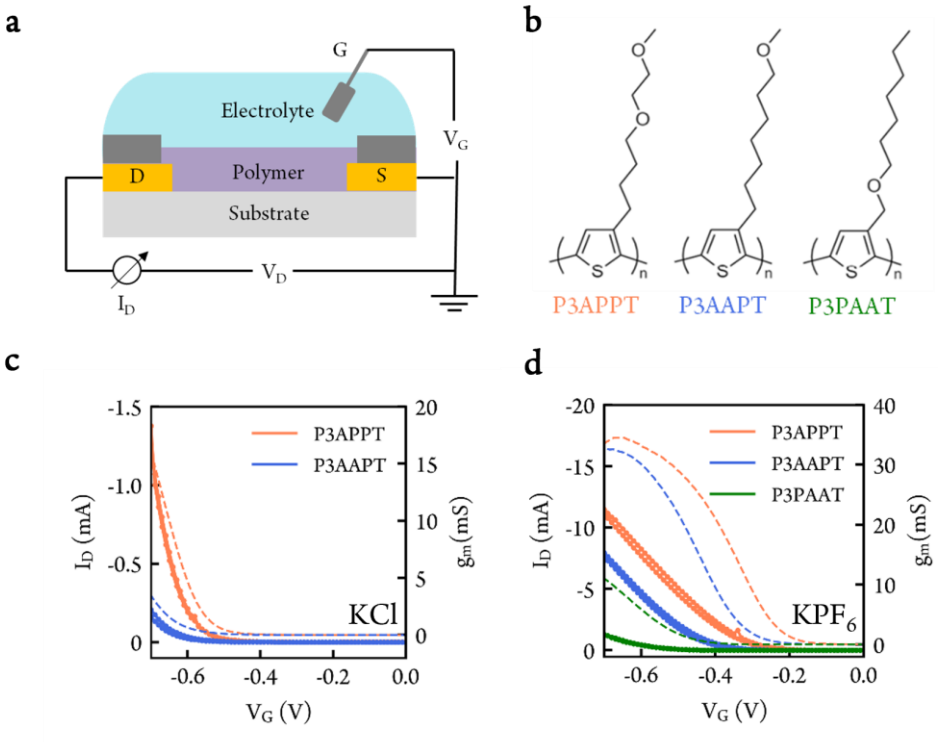

Figure 1. (a) OECT device schematic. S and D represent source and drain electrode, respectively. Insulating layer (dark grey) was applied on top of gold electrode to prevent direct contact between gold and electrolyte. A Ag/AgCl pellet was used as gate electrode (G). (b) Chemical structure of reduced-oxygen-content side chain polymers. An example OECT transfer curve (dot line) and transconductance (dash line) of reduced-oxygen-content side chain polymers in 100 mmol/L (c) $KCl_{(aq)}$ and (d) $KPF_{6(aq)}$. Transistor channel width/length = 4000 µm /10 µm. V_D = -0.6 V for all measurements.

on the side chain farther from the polythiophene backbone. Poly(3-(methoxyheptyl)thiophene), or P3AAPT, possesses one oxygen atom on the side chain farther from the polymer backbone. Poly(3-(heptoxymethyl)thiophene), or P3PAAT, has one oxygen atom on the side chain closer to polythiophene backbone. The polymers were synthesized via Kumada Catalyst Transfer Polymerization (KCTP), and all polymers have similar number average molecular mass ($M_n \approx 10$ kg/mol), degree of polymerization (DP ≈ 50) and dispersities (Đ < 2). Table 1 summarizes the polymer properties. The details of the polymer synthesis have been described previously.[31] Figure 1c and Figure 1d show the typical OECT transfer curves (W = 4000 µm, L = 10 µm) in KCl and KPF_6 solutions, respectively. We measured for V_G only up to -0.7 V (vs. Ag/AgCl) because exceeding this value could lead to rapid device degradation and even water electrolysis. P3APPT, with two oxygen atoms on the side chain, exhibits higher I_D and g_m compared to P3AAPT and P3PAAT in both KCl and KPF_6 solutions. This result indicates that more oxygen content on the side chain results in better OECT performance. Interestingly, comparing the polymers with only one oxygen per side chain, P3AAPT shows a higher I_D and g_m compared to P3PAAT in KPF_6 solution, indicating that an oxygen atom farther from the polymer backbone is more beneficial for OECT operation. Both P3APPT and P3AAPT OECT devices demonstrate higher I_D and g_m when measured with the chaotropic PF_6^- anion compared to the kosmotropic Cl^- anion, a result which is in agreement with our previous studies.[28,37] We did not observe any OECT performance of P3PAAT in KCl solution: the magnitude of I_D measured was equivalent or smaller than the gate current (I_G) (Figure S2a). This result means barely any current flows through the channel (from source electrode to drain electrode), and the device is not yet turned on. We believe that the inability to observe transistor behavior of P3PAAT with KCl as the electrolyte is because, in that case, the |threshold voltage| is > 0.7 V (vs Ag/AgCl), such that material degradation or water electrolysis occurs before the device turns on. In contrast, with a lower threshold voltage, P3PAAT becomes a working OECT device with KPF_6 (Figure S2b). This result again emphasizes the importance of the choice of counterion for OECT operation.

Table 1. Polymer properties

	P3MEEMT	P3APPT	P3AAPT	P3PAAT
M_n (kg/mol)	11.2	10.5	12.4	9.1
Đ	1.46	1.51	1.38	1.91
Optical gap (eV) [a]	2.07	1.92	1.89	2.22
Film thickness (nm)	≈ 80	≈ 77	≈ 95	≈ 94

a. See Figure S1.

To compare the performance of polymers with reduced oxygen content on the side chains to the reference polymer, P3MEEMT, we calculated the μC^* of polymers in both electrolytes using Eq. 1. Figure S3 shows the resulting μC^* fitting results while Figure S4 and Figure S5 show the output curves and confirm that the transfer curves were measured in the saturation region (V_D = -0.6 V), and it is thus feasible to apply Eq. 1 to compute μC^*. We noticed that the max g_m was not reached in KCl solution prior to the onset of irreversible electrochemical processes around ≈ -0.8 V (vs. Ag/AgCl). To maintain a fair comparison, we calculated μC^* with g_m obtained at $|V_G| - |V_T|$

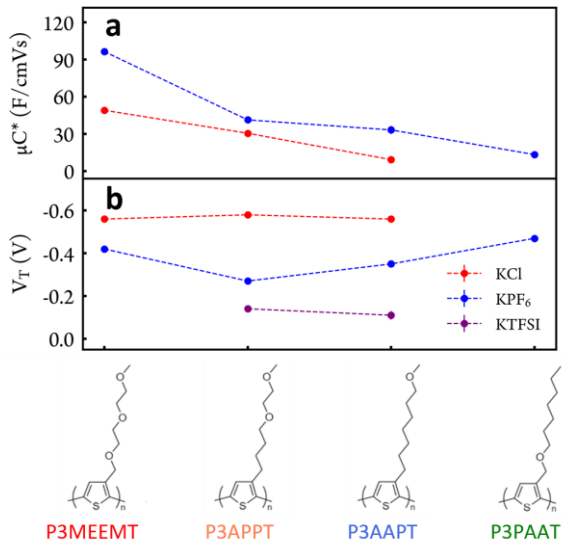

Figure 2. (a) OECT material figure of merit μC^* and (b) OECT threshold voltage (V_T) in 100 mmol/L $KCl_{(aq)}$ (red), $KPF_{6(aq)}$ (blue) and KTFSI (purple). Dash lines are guide for the eye.

≈ 0.13 V for all cases. Figure 2a shows the μC^* of four polymers in both KCl and KPF_6 solutions. With the kosmotropic Cl^- anion, we found that μC^* is very sensitive to both side chain oxygen content and position. We show that there is a positive correlation between μC^* and side chain oxygen atom content in KCl solution. For the chaotropic PF_6^- anion, we observed a similar μC^* trend as with the Cl^- anion, albeit with less sensitivity of the μC^* value to the side chain oxygen content, a result which could be explained by the more hydrophobic nature of the PF_6^- anion. We also noticed that a higher μC^* was obtained with the chaotropic PF_6^- anion compared to kosmotropic Cl^- anion for all four polymers. Overall, we show higher μC^* with more oxygen atoms on the side chain, or if the oxygen atom is farther from the polymer backbone in both KCl and KPF_6 solutions.

Previously, Luscombe and co-workers have demonstrated that P3APPT, as polymer electrolyte for LiTFSI salt, exhibits higher electronic conductivity and comparable ionic conductivity to fully-glycolated P3MEEMT.[31] The fact that P3MEEMT is still a better OECT active layer with higher μC^* compared to P3APPT indicates the very different nature of polymer/ion interaction in dry and hydrated states. And it is thus necessary to apply different design strategy for various OMIECs applications.

Figure 2b shows the threshold voltage (V_T) of the polymers in both solutions while Figure S6, Figure S7 and Figure S8 show the determination of V_T. To measure V_T, we took the intersection of the tangent line of plots of $\sqrt{I_D}$ curve (with maximum slope) and the x-axis in the $\sqrt{I_D}$ vs. V_G plots. A smaller $|V_T|$ is generally preferred for accumulation mode OECTs as the device can be turned on at lower gate voltage. Interestingly, we found the V_T of P3MEEMT, P3APPT and P3AAPT are all ≈ -0.56 V (vs Ag/AgCl) with Cl^- as the counterion. When replacing the Cl^- with PF_6^-, we observed the expected decrease of V_T for all three polymers. In addition, we found an even lower V_T of P3APPT and P3AAPT compared to P3MEEMT with PF_6^- counterion. One possible explanation is the higher crystallinity of P3APPT and P3AAPT films in the undoped state compared to P3MEEMT,[31] which enables easier hole injection to start electrochemical doping process. While with Cl^- anion, which has higher hydration number and is very sensitive to side chain hydrophilicity during doping, we hypothesize that opposite factors are at play: easier polaron injection because of the higher film crystallinity at undoped state (lower V_T), but harder Cl^- anion injection due to the lower side chain hydrophilicity (higher V_T). And the V_T of P3MEEMT, P3APPT and P3AAPT are thus all similar in KCl solution. Overall, our results clearly demonstrate that V_T is sensitive to both counterion and polymer side chain hydrophilicity, and that using the chaotropic anions (PF_6^- and $TFSI^-$) lowers the V_T compared to the kosmotropic Cl^- anion.

3.2. EIS and QCM-D Characterizations

To understand the reason behind the observed μC^* trend, we next utilized electrochemical impedance spectroscopy (EIS) to measure the volumetric capacitance C^* of the polymers. Briefly, the impedance of the polymer (gold/polymer/electrolyte) was measured through a small alternating current (AC) perturbation applied on top of a constant direct current (DC) doping bias. The impedance results were then fitted to an equivalent circuit, and the C^* was determined as the capacitor value divided by the polymer film volume. Figure S9 and Figure S10 show Nyquist plots and Bode plots of all four polymers in both KCl and KPF_6 solutions, respectively. For the reference P3MEEMT polymer, we observed only one quarter-circle in the Nyquist plot (Figure 3b) and one phase peak (at ≈ 1 Hz) in the Bode plot (Figure 3b). This result indicates only one capacitor component in the system, and a simplified Randles circuit (Figure 3a) is adequate to describe the polymer/electrolyte system.[32,33] In a simplified Randles circuit, resistance 1 (R_1) and resistance 2 (R_2) are usually interpreted to represent the solution resistance and polymer resistance, while CPE_1 represents the counterion-polaron pairs either throughout the bulk polymer film (i.e. volumetric capacitance in an OECT) or at the polymer/electrolyte interface (i.e., double layer capacitance in an electrolyte-gated organic field-effect transistor).[8] Note that we used a constant phase element (CPE) instead of a pure capacitor in the equivalent circuit. CPE is a common equivalent electrical circuit component representing an imperfect capacitor. More details about the use of the CPE and the conversion of the CPE to capacitance is described in supplemental information.

As the side chain hydrophilicity decreases, we begin to recognize two quarter/semi-circles in the Nyquist plots and two phase peaks in the Bode plots for P3APPT and P3AAPT in both KCl and KPF_6 solutions (Figure 3c, Figure 3d, Figure S9 and Figure S10). We thus applied the Kovac's circuit (Figure 3a) as the equivalent circuit because of the existence of two capacitor components in the system.[33,34] CPE_2 is typically 1 to 2 orders of magnitude larger than CPE_1 in our results. The position of the CPE_2 phase peak is smaller than 1 Hz, while the position of CPE_1 phase peak is typically larger than 100 Hz. We used CPE_2 for further C^* calculations. The two capacitor components could indicate "the inhomogeneous counterion-polaron pair formation" phenomenon proposed for polymer/electrolyte systems. One possible explanation of this phenomenon is that both double layer capacitance (interfacial doping) and volumetric capacitance (volumetric doping) coexist in the polymer/electrolyte system of some range of conditions.[30,38] This situation could arise if domains with different hydrophilicity and stiffness existed in the polymer film. The interfacial doping occurs in more hydrophobic and stiffer region,

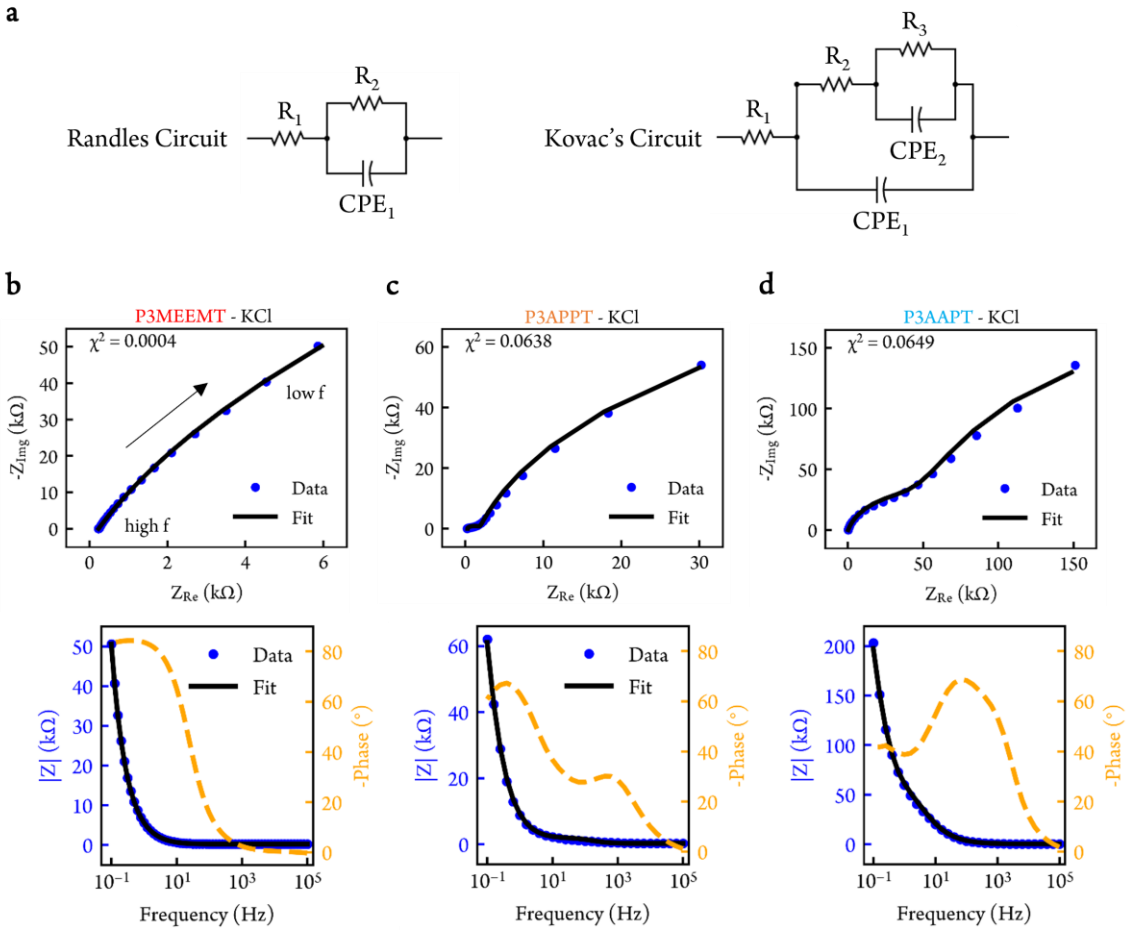

Figure 3. (a) Randles circuit (left) and Kovac's circuit (right). Resistor (R) and constant phase element (CPE). Nyquist plot (top) and Bode plot (bottom) of (b) P3MEEMT (c) P3APPT and (d) P3AAPT in 100 mmol/L $KCl_{(aq)}$.

while the volumetric doping appears in more hydrophilic and softer domain, and CPE_1 and CPE_2 represent double layer capacitor and volumetric capacitor, respectively. The 1 to 2 order(s) of magnitude difference between CPE_1 and CPE_2 supports the theory.

Alternatively, CPE_1 might represent counterion-polaron pairs formed at the crystallite/amorphous interface while CPE_2 could represent counterion-polaron pairs formed within crystalline domains when ions penetrate the crystallites at lower frequency. Previously, Thomas et al. have suggested electrochemical doping (formation of counterion-polaron pair) of poly(3-hexylthiophene) (P3HT) starts first at the crystallite/amorphous interface, followed by ion injection into the crystallites and eventually doping occurred within the crystallites.[39] Guardado et al. demonstrated counterions only penetrate the P3HT crystallites at lower frequency and tend to stay in the amorphous regions at higher frequency.[40] This explanation makes sense with the context of our data. For the reference polymer, P3MEEMT, because ions can penetrate the crystallites and approach the polymer backbone more easily due to its more hydrophilic side chain, the doping of P3MEEMT tends to occur simultaneously at crystallite/amorphous interface and within crystallites. And thus, only one capacitor component (CPE_2) is observed. As the side chain hydrophilicity decreases, the reduced-oxygen-content side chain polymers behave more like P3HT, and the doping tends to be faster at crystallite/amorphous interface, and slower within crystallites. Our previous study supports this hypothesis and shows the P3MEEMT lamellar spacing expands already when in contact with aqueous solution (easier for ion injection), while P3HT lamellar spacing only expands after a doping bias applied.[28]

For P3PAAT in KPF_6 solution (Figure S9h and Figure S10h), we also observed two capacitor components in the impedance spectrum. In contrast, for P3PAAT in KCl solution (Figure S9g and Figure S10g), we found only one smaller capacitor component with a phase peak at ≈ 100 Hz (CPE_1), indicating either only double layer capacitance exists in the polymer/electrolyte system or only counterion-polaron pairs mainly at crystalline/amorphous interface exist. We note that similar C^* results were obtained from fitting the wider range of impedance spectrum (10^5 Hz to 10^{-1} Hz) with Kovac's circuit (this work) and from fitting the impedance spectrum only at lower frequency (10^1 to 10^{-1} Hz) with RC (or R-CPE) circuit. The latter method has been commonly used in the literature.[20,41]

Figure 4a shows the volumetric capacitance (C^*) of polymers in KCl, KPF_6 and KTFSI solutions as determined via the EIS fits to the Kovac's equivalent circuit show in Figure 3, Figure S9, Figure S10 and Figure S11. The C^* is obtained at a fixed potential above threshold ($|V_{doping}| - |V_T|$) of 0.13 V (vs. Ag/AgCl) for all cases. For the

kosmotropic Cl^- anion, we found C^* is very sensitive to oxygen content and position on the side chain: we obtain larger C^* values where there are more oxygens on the side chain, or if the oxygen atom is farther from polythiophene backbone. Consistent with previous reports for hydrophobic polymers like P3HT,[37,42] we find that using more chaotropic anions like PF_6^- and $TFSI^-$ results in higher C^* overall. While the use of chaotropic anions decreasing the overall sensitivity of the C^* to the side chain structure, the same general trend holds, with P3MEEMT having the highest C^* and P3PAAT having the lowest C^*, regardless of the counter anion species. Figure S12 shows the charge injected in each polymer during three consecutive cyclic voltammetry (CV) scans in both KCl and KPF_6 solutions. Figure S13 shows the positive correlation between C^* and normalized charge injected during CV scan and verifies the C^* trend shown in Figure 4a. Table S1 summarizes the V_T and C^* results of P3APPT and P3AAPT in 100 mmol/L $KTFSI_{(aq)}$.

We further measured passive swelling of the polymers via quartz crystal microbalance with dissipation mode (QCM-D). Passive swelling tracks the polymer film thickness change upon in contact with aqueous solution (with no potential bias applied). We followed a standard procedure commonly used in the field.[17,29,43] In brief, the mass change of polymer film in between air and aqueous solution is determined from the vibrational frequency change of the quartz crystal using the Sauerbrey equation.[36] Figure 4b shows the passive swelling level of all four polymers in deionized (DI) water. We did not observe significant differences between the passive swelling levels for the polymers in DI water, in KCl, or in KPF_6 solutions. P3MEEMT has the highest passive swelling level (≈ 121 %), which agrees with our previous measurement through atomic force microscopy (AFM) (105 ± 30%).[28] P3APPT (≈ 55 %) and P3AAPT (≈ 57 %) have similar passive swelling levels. P3PAAT exhibits the lowest passive swelling (≈ 14.5 %). Comparing the passive swelling levels of P3AAPT and P3PAAT, it is clear that the oxygen atom on the farther end of side chain enables more water molecules to diffuse into polymer film, in spite of the higher crystallinity of P3AAPT compared to P3PAAT.[31] This result agrees with the previous MD and dry film studies, as an extended solvation domain is created due to the cooperative effect between the EG units on the farther end of side chain of the adjacent polymer backbones.[31] Notably, the passive swelling level is correlated to the C^* in this family of polymers, which is reasonable as more anions could migrate into the film and compensate the polaron if larger solvation domains exists in the polymer film.

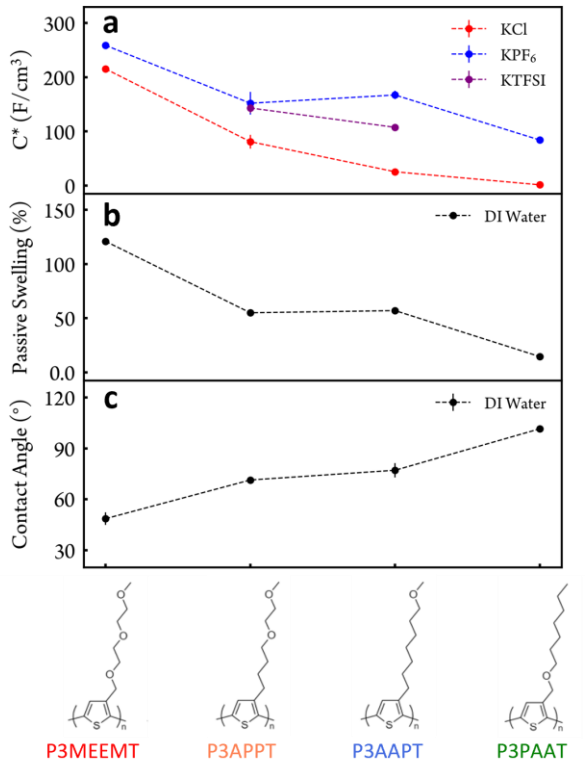

Figure 4. (a) Volumetric capacitance C^* in 100 mmol/L $KCl_{(aq)}$ (red), $KPF_{6(aq)}$ (blue) and KTFSI (purple). (b) Passive swelling of polymers in DI water. We did not observe significant difference of passive swelling in $KCl_{(aq)}$, $KPF_{6(aq)}$ or DI water. (c) Water contact angle of polymers. Dash lines are guide for the eye.

Figure 4c shows the water contact angle results of the four polymers. We found the trend of water contact angle agrees with the trend of passive swelling level, and is anticorrelated with C^* when using Cl^- anion. Among the four polymers, P3MEEMT is the most hydrophilic polymer with the lowest water contact angle (46.51 ± 3.66°) and P3PAAT is the most hydrophobic polymer with the highest water contact angle (101.53 ± 2.14°). The water contact angle of P3APPT (71.37 ± 0.32°) and P3AAPT (77.10 ± 4.16°) are similar. Figure S14 shows the contact angle measurement images of the four polymers.

Comparing the trends of μC^* and C^*, we conclude that the C^* is the dominant factor controlling the variation of OECT figure of merit across this family of polymers. This conclusion is also consistent with our observation of relatively constant hole mobilities across this family (Figure S15 shows the OECT hole mobility of the polymers). Even though P3APPT and P3AAPT have higher crystallinity in the dry film compared to P3MEEMT, [31] we did not observe significant difference in OECT hole mobility. This result, while surprising for a dry FET, is reasonable for an OECT, as the polymer film is in a hydrated state and the hole mobility is dependent on the doping level.[14,39] In summary, more oxygen content on the side chain, or having an oxygen atom on the farther end of the side chain creates larger solvation domains and results in more passive swelling and higher C^*, accounting for the predominant differences in the μC^* product for different members of this family of polymers.

3.3. Spectroelectrochemistry and Electrochemical Doping and Dedoping Kinetics

Figures S16 and Figure S17 show the UV-vis absorption spectra of the four polymers in KCl and KPF_6 solutions, respectively, under different doping potentials. We thoroughly dedoped the polymer films between each doping cycle. We found the π-π^* peak absorbance decreasing and the polaron peak absorbance increasing as the potential bias applied, vice versa when the dedoping bias was applied. This phenomenon indicates reversible doping and dedoping of polymers within the water potential window. We measured the π-π^* peak at ≈ 530 nm for both P3APPT and P3AAPT, ≈ 480 nm for P3MEEMT and ≈ 460 nm for P3PAAT. A broad polaron peak is at ≈ 750 nm for all 4 polymers. A vibronic progression feature is observed for both P3APPT and P3AAPT in the neutral and slightly doped states, which suggests increased planarization and ordering of polymer backbone as reported by Onorato et al.[31] In contrast, we did not

observe the vibronic progression feature in P3MEEMT and P3PAAT, likely because the oxygen atom closer to the polymer backbone lowers the along-backbone ordering. Upon increasing the doping bias, the ratio between the 0-0 and 0-1 vibronic features increases for both P3APPT and P3AAPT, consistent with H-type aggregates (mainly in crystalline domain) being doped prior to other regions of the film.[39,44] This observation is similar to Thomas et al.'s results with P3HT, in which they concluded the counterion-polaron pair first formed at crystalline amorphous interface, within crystalline region and lastly in amorphous domain.[39] Our spectroelectrochemistry results thus support the notion of the formation of an inhomogeneous distribution of counterion-polaron pairs within the polymer film.

Figure S18 shows the comparison of the polaron and π-π* peak absorbance change upon doping in KCl and KPF_6 solutions. Consistent with the impedance measurements discussed above, it is clear that higher doping level are achieved for all polymers with chaotropic PF_6^- as the counter anion compared to kosmotropic Cl^- as the counter anion. We also observed the π-π* and polaron peak absorbance start to change at lower potential biases with PF_6^- as the counter anion, indicating the lower doping threshold of PF_6^- anion compared to Cl^- anion. This result verifies our earlier contention that the chaotropic counter anion lowers the doping threshold and enables higher doping level of the polymers, in agreement with our EIS and OECT results.

Interestingly, we observe an isosbestic point in the UV-Vis spectra of the three reduced-oxygen-content side chain polymers in KCl solution (Figure S16). The isosbestic point implies the clear conversion of polymer between neutral state and doped state. In contrast, in P3MEEMT, we observed slightly red shift of π-π* peak and we did not observe the isosbestic point. We also did not observe an isosbestic point for all polymers in KPF_6 solution (Figure S17). Table S2 summarizes polythiophene derivatives with isosbestic points observed in the spectroelectrochemistry. We suspect the occurrence of an isosbestic point is related to either larger distance between counter anion and polaron or the abrupt polymer structure change upon electrochemical doping. Further investigation on this phenomenon is undergoing in our lab.

To investigate how oxygen content and position on the side chain affect the electrochemical doping and dedoping kinetics, we

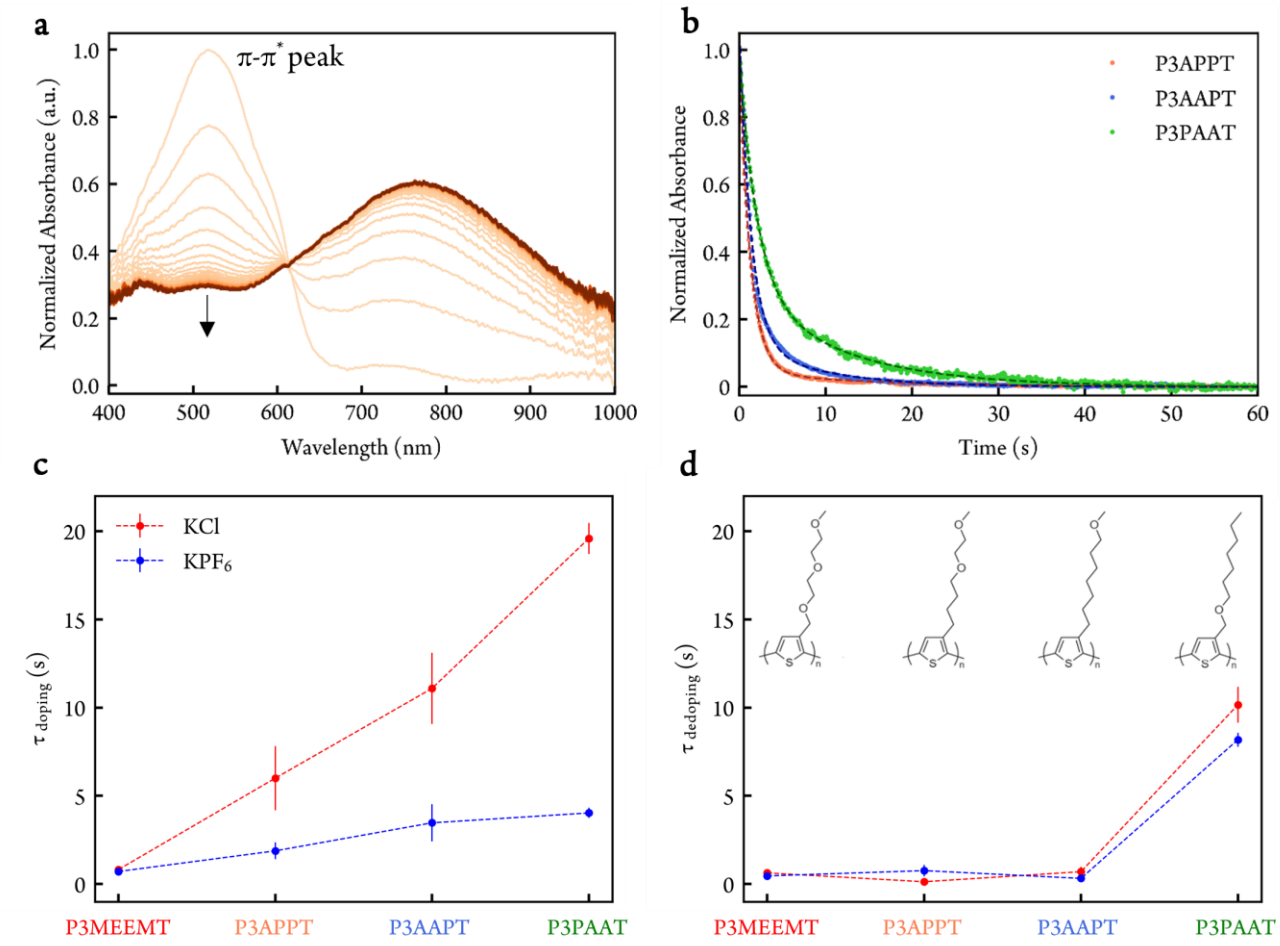

Figure 5. (a) UV-Vis spectra of P3APPT change over time when doping in 100 mmol/L $KPF_{6(aq)}$. Doping potential = 0.5 V vs. Ag/AgCl. We plotted the spectra change every 0.5 s from 0s to 60s. (b) Normalized π-π* change of P3APPT, P3AAPT and P3PAAT in $KPF_{6(aq)}$. Dash lines represent the fitting results. (c) Doping and (d) dedoping time constants of polymers in 100 mmol/L $KCl_{(aq)}$ (red) and $KPF_{6(aq)}$ (blue) via spectroelectrochemistry. Dash lines are guide for the eye. Note that P3PAAT has the lowest doping level but the doping speed is still the slowest.

Table 2. Summary of electrochemical properties of polymers in 100 mmol/L $KCl_{(aq)}$.

	μC^* [a]	C^* [b]	μ_{OECT} [c]	V_T [d]	τ_{doping} [e]	$\tau_{dedoping}$ [f]
	(F/cm·V·s)	(F/cm^3)	($cm^2/V·s$)	(V)	(s)	(s)
P3MEEMT [g]	49.1 ± 5.0	≈ 215.5	≈ 0.23	-0.56 ± 0.01	0.82 ± 0.03	≈ 0.63
P3APPT	30.5 ± 2.2	81.0 ± 12.8	0.38 ± 0.09	-0.58 ± 0.01	6.00 ± 1.82	0.13 ± 0.05
P3AAPT	9.2 ± 2.8	25.4 ± 1.7	0.36 ± 0.13	-0.56 ± 0.01	11.09 ± 2.02	0.70 ± 0.28
P3PAAT	NA	1.3 ± 0.4	NA	NA	19.59 ± 0.88	10.16 ± 1.02

Table 3. Summary of electrochemical properties of polymers in 100 mmol/L $KPF_{6(aq)}$.

	μC^* [a]	C^* [b]	μ_{OECT} [c]	V_T [d]	τ_{doping} [e]	$\tau_{dedoping}$ [f]
	(F/cm·V·s)	(F/cm^3)	($cm^2/V·s$)	(V)	(s)	(s)
P3MEEMT [g]	96.7 ± 10.2	≈ 259	≈ 0.37	-0.42 ± 0.01	0.71 ± 0.02	≈ 0.46
P3APPT	41.3 ± 2.8	152.0 ± 21.1	0.27 ± 0.06	-0.27 ± 0.01	1.88 ± 0.48	0.76 ± 0.33
P3AAPT	33.2 ± 3.3	167.2 ± 7.7	0.20 ± 0.03	-0.35 ± 0.01	3.47 ± 1.06	0.32 ± 0.06
P3PAAT	13.3 ± 1.4	84.0 ± 5.9	0.16 ± 0.03	-0.47 ± 0.01	4.03 ± 0.29	8.18 ± 0.40

a. μC^* is obtained via Eq. 1 with g_m at $|V_G| - |V_T| = 0.13$ V. $V_D = -0.6$ V. Error bars represent standard error of the mean.

b. C^* is measured at $|V_{doping}| - |V_T| = 0.13$ V. Error bars represent standard error of the mean.

c. Obtained via dividing μC^* by C^*. Error bars represent standard error of the mean.

d. See Figure S4. Error bars represent standard error of the mean.

e. Electrochemical doping time constant via spectroelectrochemistry. $V_{doping} = 0.7$ V (vs Ag/AgCl). Error bars represent standard error of the mean.

f. Electrochemical dedoping time constant via spectroelectrochemistry. $V_{dedoping} = -0.5$ V (vs Ag/AgCl). Error bars represent standard error of the mean.

g. Obtained from Flagg et al.[28]

monitored the change of π-π* peak absorbance over time when doping bias was applied (Figure 5a). Figure 5b shows the π-π* peak absorbance decreases during doping potential applied in KPF_6 solution, and in KCl solution (Figure S19a). Figure S19c, S19d show the increasing of π-π* peak absorbance when switching from doping potential to dedoping potential. To account for the doping threshold difference between the Cl^- and PF_6^- anion, the doping potential used was +0.5 V (vs Ag/AgCl) for PF_6^- anion and +0.7 V (vs Ag/AgCl) for Cl^- anion. The dedoping potential applied was -0.5 V (vs Ag/AgCl) for both anions. We used biexponential equations for fitting doping and dedoping kinetics results.

Figure 5c shows the distribution of doping time constants for eight polymer-ion pairs. Since no significant passive swelling difference was observed in KCl or KPF_6 solutions, we suggest that the initial hole mobility of the undoped polymer film is similar when in contact with KCl or KPF_6 solution. We thus propose that ion motion in the polymer film is the initial rate-determining step in the electrochemical doping process, especially for the reduced-oxygen-content side chain polymers. This result is consistent with both the counterion and side chain dependence of the kinetics. We found faster doping speed (or smaller doping time constants) with more oxygen atoms on the side chain, meaning more hydrophilic side chains facilitate faster ion motion in the polymer film. Comparing the polymers with only one oxygen atom, we find faster doping kinetics when the oxygen atom is farther from the polymer backbone (P3AAPT) compared to closer to the polymer backbone (P3PAAT). This result indicates polar functional groups farther from the polymer backbone are beneficial for ion movement in the polymer film, which is reasonable considering ions need to approach the polymer backbone from farther end of the side chain. In addition, we demonstrated faster doping kinetics with chaotropic PF_6^- anion compared to kosmotropic Cl^- anion for all four polymers, even though higher doping level is achieved with PF_6^- anion. This result is consistent with our previous studies and verifies that the bulky anion moves faster in the polymer film, possibly because the chaotropic anion is surrounded with less water molecules and is more polarizable compared to the kosmotropic anion. We also noticed that the doping speed is less affected by the side chain hydrophilicity when using PF_6^- as counter anion compared to Cl^-, likely because of the more hydrophobic nature of PF_6^- anion.

Figure 5d shows the distribution of the dedoping time constants. Though most of the studies to date focus more on doping kinetics, dedoping kinetics are also crucial, and can determine the device turn off speed in neuromorphic computing application and discharging speed in battery/supercapacitor applications. Interestingly, we find the dedoping speed is less affected by side chain oxygen content and ion species. While one might thus be tempted to attribute the dedoping kinetics to the hole mobility in the polymer, the measured dedoping time constants (≈ 10^{-1} s) are not at the correct order of magnitude if dedoping only depends on hole drifting (≈ 10^{-7} s), assuming a 1 V bias and 100 nm thick film, with a 10^{-3} cm^2/Vs mobility. A more complex process like coupled polaron-counterion movement may be involved during dedoping. Table 2 and Table 3 summarize the electrochemical properties of polymers in 100 mmol/L $KCl_{(aq)}$ and $KPF_{6(aq)}$.

Recent studies suggested that porous polymer film[42] or polymer film with nanowire architecture[23] enables faster doping kinetics. We thus conducted AFM experiments to investigate the relation between surface topography and doping kinetics. Figure S20 shows the AFM topography images of these four polymers. We found

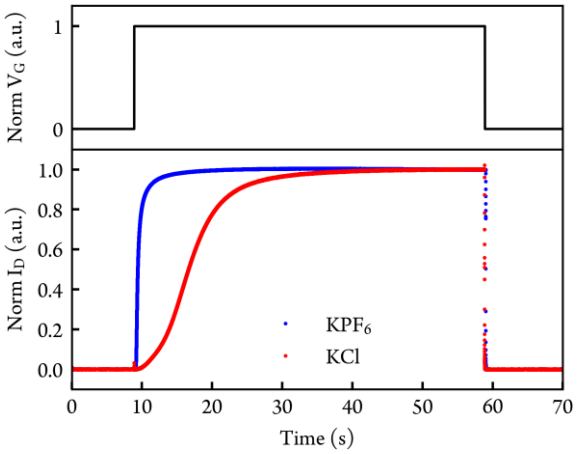

Figure 6. Comparison of OECT transient measurements of P3APPT polymer in 100 mmol/L $KCl_{(aq)}$ and $KPF_{6(aq)}$. V_D is fixed constant at -0.6 V while V_G (-0.5 V for PF_6^- and -0.7 V for Cl^-) is turned on at 9 s and turned off (0 V) at 59 s. One data point represents 1 ms. Channel width/length = 1000 μm/10 μm.

P3APPT film is smoother than P3MEEMT film, while P3AAPT and P3PAAT films are rougher than P3MEEMT. We do not find a direct correlation between film topography and doping or dedoping kinetics for this family of polymers, as such, we concluded that the kinetics trend observed in this study is not due to the film morphology difference. Figure S21 compares the roughness of neat polymer films, doped polymer films (with KPF_6), and further with polymer films doped and dedoped for three cycles with KPF_6. We did not observe significant change of polymer film roughness in these three states.

Lastly, we measured OECT kinetics with P3APPT in both KCl and KPF_6 solutions with a high time resolution capture system. Figure 6 shows the OECT transient measurement of P3APPT in KCl and KPF_6 solutions. The time resolution of the data capture is 1 ms. The drain voltage was fixed at -0.6 V and a gate doping bias was applied around 9 s and removed at 59 s. The gate voltage used was -0.5 V (vs Ag/AgCl) for KPF_6 solution and -0.7 V for KCl solution. We showed that OECT kinetics results agree with spectroelectrochemistry kinetics results: (1) doping speed is ion dependent and faster doping speed for PF_6^- anion (≈ 0.58 s) compared to Cl^- anion (≈ 9.0 s) (2) dedoping speed is less ion dependent (≈ 0.011 s for both ions) and (3) we observe a faster dedoping speed compared to doping speed. We noticed that the difference between doping and dedoping speed is further amplified in the OECT measurement compared to the spectroelectrochemistry measurement. We attribute this result to a combination of the differences in kinetics, and a difference in measurement and device geometry. In spectroelectrochemistry, the direction of polaron injection is perpendicular to the transparent, conducting FTO substrate. In contrast, polarons are injected from source electrode into channel conjugated polymer in OECT, which is parallel to the substrate. In the OECT, as soon as a small region is dedoped, the OECT turns "off", while in spectroelectrochemistry, we probe the entire concentration of polarons through the film stack.

4. Conclusions

We compared three different side chain polymers and P3MEEMT, highlighting the importance of oxygen content and its position in the side chain on many aspects of electrochemical doping and OECT operation. First, we found increasing OECT figure of merit, μC^*, and doping speed with increasing oxygen (ethylene glycol) content on the side chain, or with the oxygen atom farther from the polythiophene conjugated backbone. Second, we showed that the variations in μC^* between polymers is largely a result of variations in the C^* as a result of the oxygen content and position. Both more oxygen content on the side chain, or having the oxygen atom farther from the backbone, result in more passive swelling and higher C^*. Replacing the oxygen atom close to the polythiophene backbone with an alkyl unit increases the film π-stacking crystallinity (higher electronic mobility in the undoped film) but sacrifices the available doping sites (lower C^* in OECT). We emphasize the importance of balancing μ and C^* while designing molecular structure for OECT materials, and the necessity to develop specific molecular design strategy for different mixed ionic-electronic conducting applications. To design high μC^* material, our results indicate that single EG unit on the side chain may not be sufficient regardless of position, but farther from the backbone helps by allowing the EG units to form extended solvation domain between two adjacent polymer chains. We speculate that future designs could balance EG contents in longer side chains, focusing on small numbers of EG units in the 2-3 range, and with the EG units positioned some distance from the backbone to maintain both moderate swelling and high π-stacking crystallinity. In addition, all three reduced-oxygen-content side chain polymers exhibit higher μC^*, lower doping threshold and faster doping kinetics with chaotropic PF_6^- anion compared to kosmotropic Cl^- anion. This result is consistent with our previous studies and suggests the superiority of chaotropic anion as counterion in p-type accumulation mode OECTs. Using chaotropic counter anion may improve the OECT performances especially in neuromorphic computing application, in which faster kinetics and lower doping threshold are critical. We note that we chose all polymers to have a 9-atom-length side chain in this study to isolate the effects of the oxygen position, and further OECT studies on polymers with different side chain lengths and varying oxygen positions could thus provide more insights. Finally, we found that, compared to the doping speed, the dedoping speed is generally faster and less dependent on ion species or side chain oxygen content. These results may prove useful for the selection of polymers and polymer-ion pairing to optimize the performance of OECTs, as well as the kinetics of OECTs, organic neuromorphic circuitry, and aqueous polymer-based electrochemical energy storage.

Author Contributions

S.E.C. was responsible for conceptualization, formal analysis, investigation, visualization, writing – original draft, and writing – review & editing. L.Q.F. was responsible for formal analysis and investigation. J.W.O. was responsible for conceptualization and investigation. R.L. was responsible for investigation. J.G. was responsible for formal analysis. C.K.L. was responsible for

supervision and writing – review & editing. D.S.G. was responsible for supervision and writing – review & editing.

Conflicts of interest

The authors declare no conflict of interest.

Acknowledgements

This paper is based primarily on work funded through the National Science Foundation DMR-2003456. J.W.O. and C.K.L.'s contributions to polymer synthesis are based in part on work supported by the National Science Foundation DMREF-1922259. S.E.C. thanks the support from Clean Energy Institute (CEI) at the University of Washington. L.Q.F. thanks the support of the NIST National Research Council (NRC) associateship. We thank Dr. Rajiv Giridharagopal and Prof. Connor G. Bischak for fruitful discussions. We thank Luke Khoury and Prof. John Berg for helping with contact angle measurements. Part of this work was conducted at the Washington Nanofabrication Facility / Molecular Analysis Facility, a National Nanotechnology Coordinated Infrastructure (NNCI) site at the University of Washington with partial support from the National Science Foundation via awards NNCI-1542101 and NNCI-2025489.

Certain commercial products or company names are identified here to describe our study adequately. Such identification is not intended to imply recommendation or endorsement by the National Institute of Standards and Technology, nor is it intended to imply that the products or names identified are necessarily the best available for the purpose.

References

1 A. M. Pappa, V. F. Curto, M. Braendlein, X. Strakosas, M. J. Donahue, M. Fiocchi, G. G. Malliaras and R. M. Owens, *Adv. Healthc. Mater.*, 2016, **5**, 2295–2302.

2 K. Guo, S. Wustoni, A. Koklu, E. Díaz-Galicia, M. Moser, A. Hama, A. A. Alqahtani, A. N. Ahmad, F. S. Alhamlan, M. Shuaib, A. Pain, I. McCulloch, S. T. Arold, R. Grünberg and S. Inal, *Nat. Biomed. Eng. 2021 57*, 2021, **5**, 666–677.

3 S. Yamamoto and G. G. Malliaras, *ACS Appl. Electron. Mater.*, 2020, **2**, 2224–2228.

4 E. J. Fuller, S. T. Keene, A. Melianas, Z. Wang, S. Agarwal, Y. Li, Y. Tuchman, C. D. James, M. J. Marinella, J. J. Yang, A. Salleo and A. A. Talin, *Science.*, 2019, **364**, 570–574.

5 D. Moia, A. Giovannitti, A. A. Szumska, I. P. Maria, E. Rezasoltani, M. Sachs, M. Schnurr, P. R. F. Barnes, I. McCulloch and J. Nelson, *Energy Environ. Sci.*, 2019, **12**, 1349–1357.

6 H. S. White, G. P. Kittlesen and M. S. Wrighton, *J. Am. Chem. Soc.*, 1984, **106**, 5375–5377.

7 E. Zeglio and O. Inganäs, *Adv. Mater.*, 2018, **30**, 1800941.

8 J. Rivnay, S. Inal, A. Salleo, R. M. Owens, M. Berggren and G. G. Malliaras, *Nat. Rev. Mater.*, 2018, **3**, 17086.

9 L. Q. Flagg, C. G. Bischak, R. J. Quezada, J. W. Onorato, C. K. Luscombe and D. S. Ginger, *ACS Mater. Lett.*, 2020, **2**, 254–260.

10 X. Strakosas, M. Bongo and R. M. Owens, *J. Appl. Polym. Sci.*, 2015, **132**, 41735.

11 C. G. Bischak, L. Q. Flagg and D. S. Ginger, *Adv. Mater.*, 2020, **32**, 2002610.

12 J. Rivnay, P. Leleux, M. Ferro, M. Sessolo, A. Williamson, D. A. Koutsouras, D. Khodagholy, M. Ramuz, X. Strakosas, R. M. Owens, C. Benar, J. M. Badier, C. Bernard and G. G. Malliaras, *Sci. Adv.*, 2015, **1**, 1400251.

13 S. Inal, G. G. Malliaras and J. Rivnay, *Nat. Commun.*, 2017, **8**, 1767.

14 B. D. Paulsen, K. Tybrandt, E. Stavrinidou and J. Rivnay, *Nat. Mater.*, 2020, **19**, 13–26.

15 H. Bronstein, C. B. Nielsen, B. C. Schroeder and I. McCulloch, *Nat. Rev. Chem.*, 2020, **4**, 66–77.

16 S. M. Kim, C. H. Kim, Y. Kim, N. Kim, W. J. Lee, E. H. Lee, D. Kim, S. Park, K. Lee, J. Rivnay and M. H. Yoon, *Nat. Commun.*, 2018, **9**, 3858.

17 M. Moser, T. C. Hidalgo, J. Surgailis, J. Gladisch, S. Ghosh, R. Sheelamanthula, Q. Thiburce, A. Giovannitti, A. Salleo, N. Gasparini, A. Wadsworth, I. Zozoulenko, M. Berggren, E. Stavrinidou, S. Inal and I. McCulloch, *Adv. Mater.*, 2020, **32**, 2002748.

18 H. Y. Wu, C. Y. Yang, Q. Li, N. B. Kolhe, X. Strakosas, M. A. Stoeckel, Z. Wu, W. Jin, M. Savvakis, R. Kroon, D. Tu, H. Y. Woo, M. Berggren, S. A. Jenekhe and S. Fabiano, *Adv. Mater.*, 2022, **34**, 2106235.

19 K. Feng, W. Shan, S. Ma, Z. Wu, J. Chen, H. Guo, B. Liu, J. Wang, B. Li, H. Young Woo, S. Fabiano and X. Guo, *Angew.Chem.*, 2021, **133**, 24400– 24407.

20 M. Moser, L. R. Savagian, A. Savva, M. Matta, J. F. Ponder, T. C. Hidalgo, D. Ohayon, R. Hallani, M. Reisjalali, A. Troisi, A. Wadsworth, J. R. Reynolds, S. Inal and I. McCulloch, *Chem. Mater.*, 2020, **32**, 6618–6628.

21 C. G. Bischak, L. Q. Flagg, K. Yan, C. Z. Li and D. S. Ginger, *ACS Appl. Mater. Interfaces*, 2019, **11**, 28138–28144.

22 D. Ohayon, A. Savva, W. Du, B. D. Paulsen, I. Uguz, R. S. Ashraf, J. Rivnay, I. McCulloch and S. Inal, *ACS Appl. Mater. Interfaces*, 2021, **13**, 4253–4266.

23 R. Giridharagopal, J. Guo, J. Kong and D. S. Ginger, *ACS Appl. Mater. Interfaces*, 2021, **13**, 34616–34624.

24 X. Wu, M. Stephen, T. C. Hidalgo, T. Salim, J. Surgailis, A. Surendran, X. Su, T. Li, S. Inal, W. L. Leong, X. Wu, M. Stephen, A. Surendran, X. Su, T. Li, W. L. Leong, T. C. Hidalgo, J. Surgailis, S. Inal and T. Salim, *Adv. Funct. Mater.*, 2022, **32**, 2108510.

25 M. Moser, A. Savva, K. Thorley, B. D. Paulsen, T. C. Hidalgo, D. Ohayon, H. Chen, A. Giovannitti, A. Marks, N. Gasparini, A. Wadsworth, J. Rivnay, S. Inal and I. McCulloch, *Angew. Chemie - Int. Ed.*, 2021, **60**, 7777–7785.

26 X. Luo, H. Shen, K. Perera, D. T. Tran, B. W. Boudouris and J. Mei, *ACS Macro Lett.*, 2021, **10**, 1061–1067.

27 Y. Wang, A. Hamidi-Sakr, J. Surgailis, Y. Zhou, H. Liao, J. Chen, G. Zhu, Z. Li, S. Inal and W. Yue, *J. Mater. Chem. C*, 2021, **9**, 13338–13346.

28 L. Q. Flagg, C. G. Bischak, J. W. Onorato, R. B. Rashid, C. K.

Luscombe and D. S. Ginger, *J. Am. Chem. Soc.*, 2019, **141**, 4345–4354.

29 P. Schmode, A. Savva, R. Kahl, D. Ohayon, F. Meichsner, O. Dolynchuk, T. Thurn-Albrecht, S. Inal and M. Thelakkat, *ACS Appl. Mater. Interfaces*, 2020, **12**, 13029–13039.

30 R. Giridharagopal, L. Q. Flagg, J. S. Harrison, M. E. Ziffer, J. Onorato, C. K. Luscombe and D. S. Ginger, *Nat. Mater.*, 2017, **16**, 737–742.

31 J. Onorato, Z. Wang, Y. Sun, C. Nowak, L. Flagg, R. Li, B. X. Dong, L. Richter, F. Escobedo, P. F. Nealey, S. Patel and C. Luscombe, *J. Mater. Chem. A*, 2021, **9**, 21410–21423.

32 E. Gruz, *Discuss. Faraday Soc.*, 1947, **1**, 11–19.

33 J. H. Chang, J. Park, Y. K. Pak and J. J. Pak, *Proc. 3rd Int. IEEE EMBS Conf. Neural Eng.*, 2007, 572–574.

34 Kovacs Gregory T. A., in *Introduction to the theory, design, and modeling of thin-film microelectrodes for neural interfaces*, eds. D. A. Stenger and T. McKenna, Academic Press, New York, 1994, pp. 121–165.

35 M. Murbach, B. Gerwe, N. Dawson-Elli and L. Tsui, *J. Open Source Software.*, 2020, **5**, 2349.

36 G. Sauerbrey, *Zeitschrift fiir Phys.*, 1959, **55**, 206–222.

37 L. Q. Flagg, R. Giridharagopal, J. Guo and D. S. Ginger, *Chem. Mater.*, 2018, **30**, 5380–5389.

38 A. Laiho, L. Herlogsson, R. Forchheimer, X. Crispin and M. Berggren, *Proc. Natl. Acad. Sci. U. S. A.*, 2011, **108**, 15069–15073.

39 E. M. Thomas, M. A. Brady, H. Nakayama, B. C. Popere, R. A. Segalman and M. L. Chabinyc, *Adv. Funct. Mater.*, 2018, **28**, 1803687.

40 J. O. Guardado and A. Salleo, *Adv. Funct. Mater.*, 2017, **27**, 1701791.

41 A. Savva, R. Hallani, C. Cendra, J. Surgailis, T. C. Hidalgo, S. Wustoni, R. Sheelamanthula, X. Chen, M. Kirkus, A. Giovannitti, A. Salleo, I. McCulloch and S. Inal, *Adv. Funct. Mater.*, 2020, **30**, 1907657.

42 L. Huang, Z. Wang, J. Chen, B. Wang, Y. Chen, W. Huang, L. Chi, T. J. Marks and A. Facchetti, *Adv. Mater.*, 2021, **33**, 2007041.

43 T. Nicolini, J. Surgailis, A. Savva, A. D. Scaccabarozzi, R. Nakar, D. Thuau, G. Wantz, L. J. Richter, O. Dautel, G. Hadziioannou and N. Stingelin, *Adv. Mater.*, 2020, **33**, 2005723.

44 H. Yamagata, C. M. Pochas and F. C. Spano, *J. Phys. Chem. B*, 2012, **116**, 14494–14503.